Forward genetic screen for malignant peripheral nerve sheath tumor formation identifies new genes and genetic pathways driving tumorigenesis

Eric P Rahrmann[1,2,3,4], **Adrienne L Watson**[1,2,3,4], **Vincent W Keng**[5], **Kwangmin Choi**[6], **Branden S Moriarity**[1,2,3,4], **Dominic A Beckmann**[1,3], **Natalie Wolf**[2], **Aaron Sarver**[1], **Margaret H Collins**[7], **Christopher L Moertel**[4,8], **Margaret R Wallace**[9], **Bernat Gel**[10], **Eduard Serra**[10], **Nancy Ratner**[6], and **David A Largaespada**[1,2,3,4,8]

[1]Masonic Cancer Center, University of Minnesota, Minneapolis, MN 55455, USA

[2]Department of Genetics, Cell Biology and Development, University of Minnesota, Minneapolis, MN 55455, USA

[3]Center for Genome Engineering, University of Minnesota, Minneapolis, MN 55455, USA

[4]Brain Tumor Program, University of Minnesota, Minneapolis, MN 55455, USA

[5]Department of Applied Biology and Chemical Technology, The Hong Kong Polytechnic University, Hung Hom, Kowloon, Hong Kong

[6]Division of Experimental Hematology and Cancer Biology, Cincinnati Children's Hospital Research Foundation, Cincinnati Children's Hospital Medical Center, 3333 Burnet Avenue, Cincinnati, OH 45229, USA

[7]Division of Pathology and Laboratory Medicine, Cincinnati Children's Hospital Research Foundation, Cincinnati Children's Hospital Medical Center, 3333 Burnet Avenue, Cincinnati, OH 45229, USA

[8]Department of Pediatrics, University of Minnesota, Minneapolis, MN 55455, USA

[9]Department of Molecular Genetics and Microbiology, University of Florida, Gainesville, FL 32611, USA

[10]Institut de Medicina Predictiva I Personalitzada del Cancer, Barcelona, SPAIN

Abstract

Malignant peripheral nerve sheath tumors (MPNSTs) are sarcomas of Schwann cell-lineage origin that occur sporadically or in association with the inherited syndrome, Neurofibromatosis Type 1. To identify genetic drivers of MPNST development, we utilized the *Sleeping Beauty* (*SB*) transposon-based somatic mutagenesis system in mice with somatic loss of tumor protein p53 (*Trp53)* function and/or overexpression of epidermal growth factor receptor (*EGFR)*. Common insertion site (CIS) analysis of 269 neurofibromas and 106 MPNSTs identified 695 and 87 sites with a statistically significant number of recurrent transposon insertions, respectively. Comparison to human data sets revealed novel and known driver genes for MPNST formation at these sites. Pairwise co-occurrence analysis of CIS-associated genes identified many cooperating mutations that are enriched for in Wnt/CTNNB1, PI3K/Akt/mTor, and growth factor receptor signaling pathways. Lastly, we identified several novel proto-oncogenes including forkhead box R2 (*Foxr2),* which we functionally validated as a proto-oncogene involved in MPNST maintenance.

Malignant peripheral nerve sheath tumors (MPNSTs) are aggressive, metastatic, nerve-associated tumors, which occur sporadically (~50% cases) or in association with the inherited syndrome Neurofibromatosis Type 1 (NF1)[1]. The lifetime risk of developing a sporadic MPNST is 0.001%, compared to 5–13% for NF1 patients (1:3,000 people) where MPNSTs often arise from pre-existing plexiform neurofibromas[1,2]. Despite advances in understanding MPNST biology, the primary treatment of MPNSTs, regardless of origin, is tumor resection followed by radiation and non-specific chemotherapeutic agents resulting in 5-year survival rates of less than 25% in patients with metastatic disease[3–6]. The most commonly altered gene known to cause benign neurofibroma formation and further progression into MPNST is *NF1*, which encodes Neurofibromin 1, a RAS-GTPase activating protein that causes NF1 syndrome when mutated[7–10]. *NF1* mutation causes increased and aberrant signaling through pro-growth and pro-proliferation signaling pathways (RAS/MAPK/ERK and PI3K/AKT/mTOR) in human neurofibromas and MPNST-derived cell lines[11–13]. Overexpression of growth factor receptors and ligands like *EGFR*, *NRG*, *PDGF*, *HGF*, *SCF*, and *TGFβ1* are also observed in neurofibromas and MPNSTs with *NF1* mutation[14–19]. Besides *NF1* mutations, genomic aberrations have not been identified in neurofibromas. However, genomic aberrations including deletions and/or mutations of cell cycle regulators (TP53, RB1, and CDKN2A), gene amplification of growth factor receptors (ERBB2, EGFR, KIT, MET, and PDGFR), and the presence of hyperdiploid or near-triploid genomes commonly occur in human MPNSTs[14–33]. These observations suggest that progression to malignancy requires many cooperating genomic alterations. High levels of genomic complexity make the identification of human MPNST genetic drivers difficult and leave the following questions unanswered: 1) What gene(s) cooperate with *NF1* loss for MPNST formation? 2) What additional gene modules cooperate for MPNST formation? 3) What are the epigenetically altered drivers of MPNST formation? 4) What is the signature/identity of MPNST maintenance genes? Though some genes and genetic pathways are implicated in MPNST development, there are still many left to uncover to create effective therapies for human MPNST treatment.

Recently, the *Sleeping Beauty* (*SB*) transposon system was utilized, in a tissue-specific manner in mice, to identify genetic drivers of numerous solid and blood cancers[34–37]. To identify MPNST drivers, we targeted *SB* transposon mutagenesis to Schwann cells and their precursors using the *Cnp-Cre* transgene and a conditional *SB* mutagenesis system[35,38]. Since mutations/deletions in *TP53* and/or amplification or elevated expression of *EGFR* are commonly associated with human MPNSTs (24–75% and 25–70%, respectively), a conditional dominant-negative *Trp53*^{R270H} allele and a *Cnp-EGFR* transgene were included[23,39–42]. Analysis of 375 *SB*-accelerated PNSTs uncovered 745 common-insertion site (CIS) associated genes (known and novel). We also identified genes and signaling pathways that cooperate for MPNST formation. We identified several novel proto-oncogenes, including *Foxr2* and described new functions for *FOXR2* in human MPNST formation and maintenance. Thus, utilizing the *SB* mutagenesis system, we identified genes and genetic pathways that may provide new therapeutic targets for MPNST treatment.

RESULTS

SB mutagenesis accelerated neurofibroma development and progression to MPNST

Four experimental mouse cohorts underwent *SB* mutagenesis on wildtype or tumor pre-disposing backgrounds following *Cnp-Cre* induction in Schwann cells and their precursors (Supplementary Fig. 1a)[35,38,41,42]. Mice lacking full components for *SB* mutagenesis served as controls. Predominantly, the *Cnp-EGFR* (hereafter called EGFR-overexpressing) and *Cnp-Cre; Cnp-EGFR; Trp53*^{R270H} (hereafter called EGFR-overexpressing and p53-mutant) mice with or without *SB* mutagenesis developed nerve-associated tumors throughout the body (Supplementary Table 1, Supplementary Fig. 1b). Nerve-associated tumors possessed histological features of Schwann cell tumor stages: Schwann cell hyperplasia, benign grade 1 PNSTs (neurofibromas), and aggressive grade 3 PNSTs (MPNST in humans) (Supplmentary Fig. 1c–d). Mouse grade 3 PNSTs developed in anatomical regions observed in human MPNSTs (Supplementary Fig. 2a–b)[6,43,44]. Moreover, some control and *SB*-derived grade 3 PNSTs contained regions of divergent cellular histological subtypes and differentiation events characteristic of some human MPNSTs (Supplementary Fig. 3a–b)[45–47]. Neurofibromas displayed no divergent differentiation. Collectively, our mouse model data indicate that the common genetic changes in human MPNST produce a phenotype in mice that resembles the human disease.

To determine if *SB* mutagenesis accelerated tumor formation, *SB* expression and activity in neurofibromas and grade 3 PNSTs were first confirmed by immunohistochemistry and by PCR-excision assay (Supplementary Fig. 1e)[48]. Wildtype or p53-mutant mice undergoing transposition developed few Schwann cell tumors (~2–7%) (Figure 1a). As previously reported, EGFR-overexpressing mice developed nerve hyperplasia with low incidence of neurofibroma formation (~17%) and no grade 3 PNST formation (Figure 1a)[41]. In contrast, *SB* mutagenesis significantly enhanced neurofibroma formation (~35%, p=0.0155) and induced grade 3 PNST formation in EGFR-overexpressing mice (p=0.0141). EGFR-overexpresing and p53-mutant transgenes cooperated to significantly increase neurofibroma and grade 3 PNST formation (p<0.0001, Figure 1a). *SB* mutagenesis on both pre-disposed alleles led to neurofibroma development, significantly increased grade 3 PNST development

(p=0.0005), and significantly reduced grade 3 PNST free-survival compared to both pre-disposed alleles alone (p<0.0001, Figure 1b). Tumor penetrance for each genotype is summarized in Supplementary Table 1. Overall, *SB* mutagenesis enhanced grade 3 PNST incidence compared to controls.

Identification of Schwann cell tumor driver-mutation genes

T2/Onc insertion sites from 269 *SB*-derived neurofibromas and 106 *SB*-derived grade 3 PNSTs from 100 mice were analyzed to identify driver-mutations (CISs). We utilized two statistical methods to identify CISs: TAPDANCE CIS (td-CIS) and gene centric CIS (gCIS) analyses (See methods for details, Supplementary Data 1–2, Table 1, Supplementary Table 2)[49,50]. td-CIS analysis identified 511 neurofibroma and 34 grade 3 PNST driver-mutations with 21 genes overlapping. gCIS analysis identified 535 neurofibroma and 75 grade 3 PNST driver-mutations with 32 genes overlapping. Accounting for coinciding CISs from each analysis, there were 87 grade 3 PNST (25.3% overlap) and 695 neurofibroma driver-mutations (50.1% overlap) with 37 genes common to both tumor types.

Analysis of td-CIS association with tumor type identified significant driver-mutations in neurofibromas (n=47) and grade 3 PNSTs (n=10) (Table 1, Supplementary Table 2, Supplementary Fig. 4a–b). Known Schwann cell tumor suppressor genes (TSG), *Nf1* and *Pten*, were significantly associated with grade 3 PNSTs and identified in 34.9% (p=8.04E-06) and 30.2% (p=3.85E-06) of tumors, respectively[13,51]. In neurofibromas, *Nf1* and *Pten* insertions contributed to 16.4% and 14.1% of tumors, respectively. The most commonly mutated neurofibroma CISs were *Csmd1* (46.8%, p=1.12E-05), *Utrn* (30.5%, p=0.02189) and *Zbtb20* (29.4%, p=1.15E-05). Genes previously implicated in human MPNST formation were also identified: *Bmpr2* (9.4%, p=0.005), *Jak2* (5.7%, p=0.0013), and *Nf2* (5.7%, p=0.0013).

The position/orientation of the T2/Onc murine stem cell virus (MSCV) promoter relative to the direction of gene transcription can be used to predict whether T2/Onc is likely to drive or disrupt gene transcription[52]. Transcriptional activation may occur if the majority of transposon insertions are orientated upstream of a gene or translational start site with MSCV promoters in the same direction as gene transcription; the gene would be a putative proto-oncogene (e.g. *Eras*, *Foxr2*, and *Zfp521)* (Supplementary Fig. 5a, Supplementary Table 3). Disruption of transcription may occur if the transposons land within a gene with no MSCV promoter orientation or insertion site bias within the locus; the gene would be a putative TSG (e.g. *Nf1* and *Pten*) (Supplementary Fig. 5b, Supplementary Table 3). Twenty putative proto-oncogenes and sixty-seven putative TSGs were identified in grade 3 PNST CISs (Table 1, Supplementary Table 3).

Comparative analysis of grade 3 PNST CISs identified novel genes involved in MPNSTs

Relevance of the CIS-associated genes to human MPNST formation was evaluated by cross-species comparative analysis of the grade 3 PNST CISs to previously generated human array comparative genomic hybridization (aCGH), single nucleotide polymorphism (SNP) arrays, human microarray expression, and methylome data from normal Schwann cells, neurofibromas, and MPNSTs (Figure 2)[5,53,54]. Utilizing human MPNST aCGH data, we

identified CISs with a tendency toward CNA-gains (n=31, *ZBTB10, CDK13, RAB2A, SHFM1, CPNE3*) and CNA-losses (n= 34, *CDKN2A, JAK2, NF1, NF2, FAF1, PLAA, PICLAM*) (Supplementary Table 4, Figure 2, Supplementary Fig. 6–7)[54]. Comparably, whole genome SNP analysis on additional MPNSTs (n=14) identified several CISs in chromosomal regions gained (*BMPR2, CPNE3, EML4*) and lost (*CDKN2A, JAK2, PLAA*) in >35% of the samples (Supplementary Table 5). However, many recurrently gained/lost genes were found in regions of large chromosomal rearrangements making it difficult to discern whether they are driver or passenger mutations. To address this concern, methylome and microarray expression data from human Schwann cell tumors were analyzed.

Promoter CpG Island Shore (CpG-IS) methylation status is predictive of gene expression: hypermethylation is associated with gene silencing and hypomethylation is associated with gene expression[53]. We used MPNST whole methylome data to analyze the methylation patterns of the promoter CpG-IS regions[53]. Fifty-five CIS genes showed significant differential hypo- or hyper-methylation patterns in their CpG-IS regions (see Online Methods, Supplementary Table 6, Figure 2). Six CISs displayed hypomethylation in >10% of tumors (*BMPR2, PRDX1, PTPN14, BAZ1B, JMY, MAEA*), while only *KLF13* was hypermethylated in >10% of MPNSTs.

To assess the impact of CNAs and methylation patterns on gene expression, we utilized microarray expression data. Seventy-seven CISs had a human homolog on the microarray (Supplementary Fig. 8)[5]. Microarray expression data predict CISs either upregulated (*EIF4ENIF1, EML4, PTCH1, TRIP10, ZBTB10, ZNF217, ZNF521*) or downregulated (*TAOK1, PICALM, NF1, NF2, SPAG9, SRGAP2, PTEN*) in disease progression to MPNSTs (Supplementary Fig. 8, Figure 2). Overall, genes we predicted to be oncogenes and TSGs from the SB screen displayed the expected biases in overexpression/CNA-gains/hypomethylation and reductions in gene expression/CNA-losses/hypermethylation (Figure 2). These genes include known drivers of MPNST formation (*CDKN2A, PTEN, NF1*) and novel candidate drivers (*BAZ1B, FOXR2, ERAS, PLAA, DIP2C, PICALM*).

Lastly, we utilized the catalog of somatic mutations in cancer (COSMIC-v63) database to assess alterations of the CISs in other human cancers (Supplementary Table 7)[55]. The grade 3 PNST CIS list is significantly enriched for in the Cancer Gene Census (12/488 genes, FET p=2.99×10^{-06}, hypergeometric test p=3.206496×10^{-06}) indicating we identified driver-mutations common to many cancer types.

MPNST candidate genes are enriched in specific signaling pathways and processes

Ingenuity Pathway Analysis (IPA) and the Database for Annotations, Visualization and Integrated Discover (DAVID) were used to identify significantly altered signaling pathways in grade 3 PNST CISs (Supplementary Tables 8–9). IPA identified significant enrichment in cancer-associated signaling pathways (p=8.69×10^{-09}–3.89×10^{-03}, n=25 genes) including PI3K/AKT (p=1.55×10^{-03}), ERK/MAPK (p=3.79×10^{-02}), Wnt/CTNNB1 (p=5.20×10^{-04}) and BMP/TGF-β (p=4.15×10^{-02}). Cell cycle regulation was the most significantly altered pathway (n=21 genes, p=9.87×10^{-07}-3.89×10^{-03} and n=6 genes, FET p=2.85×10^{-05}, respectively). Additional cancer-associated signaling pathways included Jak-STAT (FET p=5.90×10^{-03}) and TGF-beta (FET p=8.40×10^{-03}). Combining data from DAVID analysis,

IPA, and literature reviews, we classified the CISs into three major signal transduction pathways implicated in MPNST development: PI3K/AKT/mTOR (16.1%), MAPK/ERK/JNK/p38 (21.8%), and Wnt/CTNNB1 (17.2%) (Figure 3a)[51,56–58]. Seven CISs (*Bmpr2, Cbp, Dyrk1a, Mark2, Mycn, Ppp2r2a, Pten*) are involved in signaling through all three pathways as canonical members and/or effectors.

Co-occurring CISs in grade 3 PNSTs

Co-occurrence analysis was performed to identify genes frequently mutated together in grade 3 PNSTs at a higher frequency than expected by chance[49]. Co-occurrence analysis of the 34 td-CISs identified 99 pairs of co-occurring CISs (co-CIS) (Supplementary Table 10). Several genes were identified as co-CISs with the known MPNST driver *Nf1: Pten*, *Dyrk1a*, *Ppp6r3*, *Taok1*, *Picalm*, *Top2b*, *Srgap2*, and *Ccny* (Supplementary Table 10, Figure 3b). *Nf1* and *Pten* were present in the highest percentage of tumors as single CISs (34.9% and 30.2% respectively, Table 1) and co-occurred in 13/106 grade 3 PNSTs (FET p=7.05×10^{-05}) compared to 1/269 neurofibromas (Figure 4a). Human microarray expression data demonstrated a reduction in *NF1* and *PTEN* with disease progression to MPNSTs. (Supplementary Fig. 8). These data suggest that co-occurring mutations in *Nf1* and *Pten* cooperate to form grade 3 PNSTs and may cooperate in human MPNST progression.

To address whether *Nf1* and *Pten* mutations cooperate to form Schwann cell tumors *in vivo*, we generated transgenic mice with biallelic inactivation of *Nf1* and heterozygous loss of *Pten* in *Cnp-Cre* expressing cells. *Cnp-Cre; Nf1$^{f/f}$; Pten$^{f/+}$* mice had a significantly decreased median survival of 101 days compared to control *Cnp-Cre; Nf1$^{f/f}$* (185 days, Logrank p=0.017) and *Cnp-Cre; Pten$^{f/+}$* (323 days, Logrank p<0.0001) mice (Figure 4b). *Cnp-Cre; Nf1$^{f/f}$; Pten$^{f/+}$* mice (n=5) succumbed to paralysis-related deaths with peripheral nerve hyperplasia and tumors, the majority of which were grade 1 neurofibromas (Figure 4c). Importantly, grade 1 neurofibromas in the extremities (sciatic nerve, brachial plexus) contained regions of high-grade PNST histology (Figure 4d). *Cnp-Cre; Nf1$^{f/f}$* mice (n=4) developed nerve hyperplasia and neurofibromas but no high-grade PNSTs. *Cnp-Cre; Pten$^{f/+}$* mice (n=15) developed hematopoietic malignancies rather than Schwann cell-related phenotypes.

These data are consistent with our previous experiments in which *Dhh-Cre; Nf1$^{f/f}$; Pten$^{f/+}$* mice only developed neurofibromas, while *Cnp-Cre; Nf1$^{f/f}$; Pten$^{f/+}$* mice had shorter median survival and possessed regions of high-grade PNST development[59]. Both mouse models demonstrate the cooperativity of *Nf1* and *Pten* mutations for accelerating Schwann cell tumorigenesis. Additional cooperating mutations identified in the co-occurrence analysis may provide insight into cooperating signaling pathways that promote MPNST formation in humans.

The novel proto-oncogene *FOXR2* has a role in human MPNST maintenance

Foxr2 is a grade 3 PNST CIS predicted to be a proto-oncogene due to the orientation and position of T2/Onc insertions (Figure 5a). mRNA fusion transcripts between the T2/Onc MSCV promoter/SD and *Foxr2* were identified in tumors with T2/Onc insertions in the *Foxr2* locus (Figure 5b). The sequenced products demonstrated splicing from the T2/Onc

splice donor into each exon of the *Foxr2* gene, including a cryptic exon not previously annotated in intron 2 (labeled 2′) (Figure 5a–b). T2/Onc fusion transcripts led to increased *Foxr2* mRNA and protein expression in tumors and tumor-derived cell lines, suggesting that *Foxr2* functions as a proto-oncogene (Figures 5c–e).

Immunohistochemical analysis of a human tissue microarray demonstrated increased cytoplasmic FOXR2 expression in MPNSTs compared to neurofibromas (Figure 6a–b). *FOXR2* mRNA and protein levels were increased in MPNST cell lines compared to normal Schwann cells and *CDK4/TERT* immortalized human Schwann cells (iHSCs) (Figure 6c)[59]. MPNST cell lines also demonstrated cytoplasmic FOXR2 expression (Figure 6d).

FOXR2 is a novel gene with unknown function. To explore the role of *FOXR2* in MPNST formation, we developed constructs to overexpress the full-length cDNA or knock out the gene using TAL-effector nucleases (*TALENs*) (Supplementary Fig. 9a–b) in iHSCs and MPNST cell lines[5,59]. *FOXR2* overexpression in the iHSC clone HSC1λ increased total FOXR2 protein and cytoplasmic staining, minimally increased *in vitro* proliferation, and significantly increased soft-agar colony formation compared to luciferase control (two-tailed t-test p<0.0001) (Figure 7a–c, Supplementary Fig. 10a). Xenograft experiments demonstrated no tumor formation in the control HSC1λ cells, but 3/5 mice harboring *FOXR2* overexpressing cells developed a tumor (Supplementary Fig. 11a–b). This phenotype was confirmed by TALEN-mediated targeted knockout of *FOXR2* in S462-TY and STS26T human MPNST cell lines (Supplementary Fig. 9b). TALENs that generated knockout or heterogeneous mutations (called mutation detected) of *FOXR2* caused loss of protein by western blot analysis (Supplementary Fig. 9c, Figure 7d). *FOXR2* knockout and mutation detected cell lines had reduced proliferation and significant reductions in colony formation ability compared to *HPRT* knockout control cells (t-test p<0.0001) (Supplementary Fig. 10b–c, Figure 7e). Additionally, *FOXR2* loss inhibited the ability of STS26T cells to form tumors in xenograft experiments compared to *HRPT* knockout controls (Figure 7f). shRNA-mediated *FOXR2* knockdown in STS26T and S462-TY cell lines confirmed the *FOXR2* TALEN results *in vitro* (Supplementary Fig. 10d–e). Collectively, *FOXR2* has minor effects on proliferation *in vitro,* whereas effects on anchorage independent growth and tumorigenicity are more profound.

DISCUSSION

We performed a large, forward genetic screen in Schwann cells utilizing *SB* somatic cell mutagenesis. We identified hundreds of genes that cooperated with *EGFR* overexpression and p53-loss of function to form neurofibromas and grade 3 PNSTs. Many co-CISs were identified, suggesting that specific, cooperating genetic mutations are required for tumor development. Also, CISs were identified in known signaling pathways altered in human MPNSTs: Wnt/CTNNB1, PI3K/Akt/mTor, and growth factor signaling[11–13,58]. Lastly, we identified several novel proto-oncogenes, including *Foxr2,* and elucidated a role for *FOXR2* in human MPNST maintenance.

SB mutagenesis alone or on the *Trp53^{R270H}* background was insufficient for Schwann cell tumorigenesis compared to previous reports in which *SB* alone caused tumors[35,60]. This may

be explained by differences in the number of cells susceptible to *SB* mutagenesis. Compared to colonic epithelial cells, which have a high turnover rate, that of Schwann cells is near zero unless injury occurs[60,61]. Moreover, *SB* mutagenesis is a random event, and mutations that confer selective advantage for clonal outgrowth are rare events. Taken together, targeting a small population of cells with a low turnover rate may produce fewer *SB*-induced tumors unless a pre-existing mutation(s), such as EGFR-overexpression, is present to expand target cell populations[41].

CIS overlap between two methods for defining CISs in grade 3 PNSTs and neurofibromas was 65% and 68%, respectively (Table 1, Supplementary Table 2). The discordance in CIS calling is based predominantly on methods used to identify a CIS[49,50]. gCIS analysis is based on window sizes corresponding to annotated genes and 15,000bp upstream to account for the promoter region[50]. Therefore, the number of insertions required to be deemed a gCIS depends on gene size (i.e., large genes require many insertions while smaller genes require fewer insertions). TAPDANCE analysis generates random window sizes throughout the genome and does not require gene annotation to identify CISs, as 4 'gene barren' regions were identified in the neurofibroma CIS list (Supplementary Table 2)[49]. These regions could contain important enhancer elements, unannotated genes, non-coding RNAs, or other gene regulatory elements. The two methods are complimentary and enhance CIS identification.

Based on the number of neurofibromas (n=269) and grade 3 PNSTs (n=106) sequenced, there is a disproportionate number of CISs between neurofibromas (695) and grade 3 PNSTs (87). Analysis of unique transposon insertion site non-redundant (nr) regions identified 33,022 and 139,543 nr-regions for grade 3 PNSTs and neurofibromas, respectively. This discrepancy can be reconciled by the genetic heterogeneity of the *SB*-induced tumors. The fewer grade 3 PNSTs nr-regions were sequenced at a higher frequency compared to the neurofibroma nr-regions, suggesting that few cells acquired mutations in strong genetic drivers that conferred a selective advantage for clonal outgrowth. These clonal insertions were sequenced thousands of times more than in the more genetically heterogeneous neurofibromas. Additionally, it is possible only a few, strong driver mutations in Schwann cells are required for progression to grade 3 PNSTs, while there are many alterations that are sufficient to cause neurofibroma formation. For example, cells may achieve many mutations but only the right combination of two or more genes may drive high-grade tumor formation, as we observed in the *Nf1/Pten* model. Lastly, we can reliably identify low-penetrant CISs with higher statistical power given the larger neurofibroma sample size compared to the grade 3 PNSTs.

CIS analysis identified a disproportionate number of putative TSGs compared to proto-oncogenes (Table 1, Supplementary Table 2), which also occurred in other solid tumor SB screens[34,60,62] and likely has several explanations: 1) The strength of the T2/Onc MSCV promoter is not strong enough to sufficiently transcriptionally activate proto-oncogenes. A body-wide SB screen using the CAGGs promoter instead of MSCV in T2/Onc identified a larger spectrum of tumors and CISs[35]. 2) T2/Onc can insert in both orientations with less insertion position bias within or near a gene to cause inactivation meaning a greater chance of genes being inactivated. Alternatively, for driving oncogenes we observed a clustering of

T2/Onc insertions in the promoter region or 5′UTR that predominantly orient to drive transcription.

Comparative genomic analysis reliably identified genes previously implicated in human MPNST formation (i.e., *CDKN2A*, *NF1*, *PTEN*)[27,63]. We also identified novel genes recurrently overexpressed/CNA-gains/hypomethylated (*BAZ1B, FOXR2, ERAS*) and underexpressed/biallelically inactivated/hypermethylated (*DIP2C, PLAA, PICALM*) in human MPNSTs (Figure 2, Supplementary Figs. 6–8, Supplementary Tables 4–6)[63,64]. However, we identified genes (e.g., *ZBTB10* and *EML4*) with CNA gains in human MPNSTs predicted to be disrupted by SB mutagenesis. This discrepancy may reflect differences in mouse versus human MPNST formation and/or CNAs observed in human MPNSTs may mask the function of the gene in tumor progression. Additionally, many of the CISs could be categorized into signaling pathways (PI3K/AKT/mTOR, MAPK/ERK/JNK/p38, and Wnt/CTNNB1) (Figure 3a, Supplementary Tables 8–9). Collectively, these data provide novel gene drivers/signaling pathways that potentially promote human MPNST formation. Further experimental evidence is required to determine the contribution any candidate driver gene(s)/pathways may have on MPNST development.

Nf1 and *Pten* were most frequently mutated in our screen*,* and *Pten* was significantly co-mutated with *Nf1* in grade 3 PNSTs. Loss of *NF1* alone is not sufficient for MPNST formation in genetically engineered mouse models of *Nf1* loss[65–68]. Gregorian et. al demonstrated that monoallelic inactivation of *Pten* in Schwann cells with activated *KRas*^{G12D} overexpression caused grade 3 PNST formation[51]. Neither mutation alone was sufficient to generate grade 3 PNSTs. These data suggest that, like *Nf1*, *Pten* mutations alone are insufficient for MPNST formation. Our mouse model of biallelic *Nf1* inactivation and *Pten* heterozygosity demonstrated cooperation for high-grade PNST formation compared to loss of either allele alone (Figure 3a–d). We attempted to generate biallelic loss of *Nf1* and *Pten* with the *Cnp-cre* model, but no live mouse originated from the crosses with the expected Mendelian ratio of 1:8. *Cnp-Cre; Nf1$^{f/f}$; Pten$^{f/f}$* may be embryonic lethal. However, *Nf1* loss in the context of *Pten* heterozygosity produced tumors with regions containing high-grade PNSTs, which is consistent with the observation that *PTEN* expression is not completely lost in human MPNSTs. The previously reported *Dhh-Cre; Nf1$^{f/f}$; Pten$^{f/+}$* mouse model presented with neurofibromas and required biallelic inactivation of the second *Pten* allele for high-grade PNST formation[59]. Therefore, it is important to consider gene dosage, co-mutations, and timing of mutation induction to determine effective mouse models for developmental and therapeutic studies.

FOXR2 is a forkhead-box (FOX) transcription factor family member identified *in silico* on chromosome Xp11.21 in humans. *FOXR2* is an ortholog of *FOXR1* that shares 57.7% amino acid identity[69]. FOXR1 is a transcriptional inhibitor of FOX family target genes such as *p27Kip1*[70]. Similar to *FOXR1*, *FOXR2* is expressed in mouse embryonic development (E9.5) with reduced expression in adult tissues[69]. Human Protein Atlas and ONCOMINE indicate FOXR2 expression is low and variegated in normal adult human tissues, but expression is increased at the genomic (CNA gains) and protein levels in several cancers[71–73]. COSMIC-v63 reports 18 point mutations within *FOXR2* from 4,862 samples[55]. We utilized the MutationAssessor program to determine the functional impact of

the 18 point mutations on cancer, which ranged from neutral to medium with 4 point-mutations identified in the Fork-head DNA binding domain (Supplementary Table 12). This may indicate that *FOXR2* mutations are not as pivotal to cancer formation as increased expression. Our comparative genomic analysis and functional data predict that *FOXR2* is a proto-oncogene in human MPNST maintenance. FOX superfamily members have been implicated in human cancers through mechanisms like gene amplifications and translocations[74]. Further studies are warranted to determine the extent of FOXR2 involvement in tumor development and its function in normal somatic cells.

Interestingly, in the grade 3 PNSTs containing *T2/Onc-Foxr2* fusion transcripts we observed splicing into the first annotated exon of *Foxr2* where splice acceptor elements were not previously described (Figure 5). We identified RNA splicing elements (branch point 'A', polyprimidine tract, and 'AG' boundary) within 35 nucleotides of the first annotated *Foxr2* exon indicating the potential for splicing. Furthermore, *FOXR2* full-length cDNA unexpectedly encodes two unique protein isoforms (Figure 7b,d), and we observed a bias in isoform loss following TALEN knockout (Figure 7d). The *FOXR2* locus contains five in-frame methionines of which four have optimal Kozak sequences (amino acid positions 1, 25, 53, 58, and 81) with the following predicted molecular weights: 35.93kDa, 32.94 kDa, 29.76kDa, 29.17kDa, and 26.81kDas. Further studies are necessary to define the Foxr2 locus in mouse and human and to determine the implications of the use of the alternative start codons in tumorigenesis.

Overall, using a *SB* forward genetic screen we identified hundreds of candidate cancer driver genes that promote Schwann cell tumorigenesis. Moreover, we determined a new functional role for the novel proto-oncogene *FOXR2* in human MPNST maintenance. Further functional testing of additional CISs may reveal new genetic pathways to target for treatment of human MPNSTs.

URLs

Ingenuity Pathway Analysis, http://www.ingenuity.com; Catalogue of Somatic Mutations in Cancer - COSMIC, http://www.sanger.ac.uk/genetics/CGP/cosmic/; Oncomine, http://www.oncomine.org/; Database for Annotation, Visualization and Integrated Discovery – DAVID, http://david.abcc.ncifcrf.gov; gene centric CIS analysis, http://ias.eng.uiowa.edu/uploader/; UCSC Genome Browser, http://genome.ucsc.edu; Mutation Assessor program, http://mutationassessor.org/, TALE-NT (https://boglab.plp.iastate.edu/node/add/talen)

ONLINE METHODS

Transgenic animals and tumor isolation

Three transgenes were used to induce SB mutagenesis in Schwann cells: a conditionally expressed *SB* transposase enzyme (*R26-lsl-SB11*)[35], a Schwann cell specific Cre-recombinase controlled by the CNP promoter (*Cnp-Cre*)[38], and a concatomer of oncogenic transposons (T2/Onc15)[48]. Triple transgenic mice (*Cnp-Cre; R26-lsl-SB11; T2/Onc15*) undergo insertional mutagenesis in Schwann cells. MPNST predisposing alleles, *Cnp-EGFR* and conditional *Trp53^{R270H}* alleles, were also included[41,42]. Mouse cohorts are shown in

Figure 1a. Genotyping PCR was performed on phenol-chloroform extracted mouse-tail DNA as previously described[34,38,41,42].

Peripheral nerves and tumors were resected, assessed, and histologically evaluated as previously described[59]. Each sample was pathologically graded using established criteria for tumors generated in genetically engineered mouse models (GEMM)[75]. Grade 1 PNSTs are called neurofibromas. Tumors with features of human MPNSTs (GEMM grade 3 PNSTs) are called grade 3 PNSTs.

Transposon Insertion Site Analysis

DNA isolated from *SB*-derived neurofibromas and grade 3 PNSTs underwent linker-mediated PCR to amplify transposon-genomic DNA junctions and were sequenced as previously described[34]. Identification of TAPDANCE CISs and gene centric CISs from sequenced transposon-genomic DNA PCR products was performed as previously described[49,50]. The local-hopping phenomenon of T2/Onc was accounted for by excluding chromosome 15 (T2/Onc donor locus) from the analysis. Known CIS artifacts originating from the T2/Onc sequence elements (*En2*, *Foxf2*) and amplified regions of the mouse genome (*Serinc3*, *Sfi*) were also excluded[48,49]. Thirty-three histologically normal nerves from SB mutagenized mice were sequenced to assess potential transposon integration hotspots; no CISs were identified.

Gene expression data analysis

Published data (GEO accession #:GSE14038, Affymetrix GeneChip HU133 Plus 2.0) were used for gene expression pattern analysis. For gene annotation, custom CDF (custom GeneChip library file) based on RefSeq target definitions (Hs133P REFSEQ Version 8) was downloaded and used to provide accurate interpretation of GeneChip data[76].

Statistical comparisons were done using R/Bioconductor packages and GeneSpring GX v7.3.1 (Agilent Technologies). Differentially expressed (DE)-genes were defined as genes with expression levels at least three-fold higher or lower in target groups (MPNST) compared to normal human Schwann cells (NHSCs) after applying Benjamini and Hochberg false discovery rate correction (FDR/BH p ≤ 0.05)[77].

MPNST whole-methylome data analysis

Feber et al. published unbiased whole-methylome data of NHSCs, neurofibroma, and MPNST genomes (GEO accession #: GSE21714)[53]. We adopted the Feber et al. method for detecting differentially methylated regions (DMR) in MPNST compared to NHSC[53,78]. Briefly, Batman methylation scores per 100bp were averaged for each 1Kb window. A conservative threshold for DMR calling was used based on the 95th percentile of the difference in methylation score. DMR regions were mapped to human genome hg18 version (Build NCBI-36).

The nearest CpG island shores (CpG-IS) to the transcription start sites (TSS) of each gene/ miRNA were scanned[53,78]. We defined CpG-IS as areas up to 2Kb distant from CpG islands. We considered the nearest upstream CpG-IS from the transcription start site, within

5K bp ranges from each TSS. The genomic coordinates of miRNAs, genes, and CpG islands (NCBI36/hg18) were extracted from corresponding tracks of UCSC Genome Browser (http://genome.ucsc.edu). For intragenic miRNAs, we assumed their expression is influenced by the nearest CpG-IS to the TSS of their host gene.

Copy number alteration (CNA) data analysis

CNA data on 51 primary MPNSTs were from the published GSE3388 data set (Agilent Human Genome CGH Microarray kit (4x44K)[54,79]. A circular binary segmentation (CBS) algorithm was applied to the log2 ratios of intensity values from tumor and normal to reduce local noise effects. CBS calculates a likelihood-ratio statistic for each array probe by permutation to locate change-points[80]. After segmentation step, CGHcall algorithm was used to assign each segment an aberration label: gain, loss, or normal[81]. A visualization program was written in R to present overall gain/loss patterns of all 51 MPNSTs. We considered a given genomic region as significantly recurrent CNA region if the number of CNA labels (gain or loss) given to them exceeded a threshold of statistical significance that we estimated using a permutation test. Briefly, CNA labels, three state calls (gain/loss/ normal) by CGHcall algorithm, of the targets were permuted 10,000 times to get distribution, and sums of gain or loss labels were computed for each target. The 95th percentile values for both sums (23 patients out of 51) were chosen as thresholds of statistically significant recurrent CNA. Genomic coordinates used in plots were based on hg19/GRCh37.p8 (R/Bioconductor biomaRt package)[82].

SNP-Array Analysis

SNP-array analysis was performed on 14 MPNST primary tumors using the Illumina Infinium technology (Illumina, San Diego, CA). Tumors were analyzed using the Illumina Human660W-Quad beadchip. The data were processed with GenoCNA to segment the genome and determine copy number status[82].

Tissue Microarray

Representative areas of disease were identified on hematoxylin and eosin-stained sections for 30 dermal neurofibromas, 31 plexiform neurofibromas, and 32 MPNSTs. Blocks consisting of duplicate 1.0 mm core samples were constructed with a manual tissue arrayer (MTA-1, Beecher Inc, WI) with 64 cores per recipient block. Immunohistochemistry (IHC) for FOXR2 (1:100, SIGMA) was performed utilizing an immunohistochemical staining platform (Nemesis 7200, Biocare) following standard IHC protocols[83]. Digital images of IHC stained TMA slides were obtained as previously described by Rizzardi et al. 2012[84].

Cell Culture/Assays

Immortalized human Schwann cells (iHSCs) were acquired from the laboratory of Dr. Margaret Wallace. iHSCs and human MPNST cell lines (ST88-14, STS26T, S462, S462-TY, and T265) were cultured in complete media (1xDMEM, 10% fetal bovine serum, 1x penicillin/streptomycin) and grown at 37°C in 5% CO_2. shRNA GIPZ lentiviral constructs were purchased from Openbiosystems. Proliferation assays were setup in a 96-well plate format with 500 cells per well in full DMEM media containing 1ug/ml of puromycin (Life

Technologies). Proliferation was assessed every 24 hours for 5 days using the MTS assay (Promega) following the manufacturer's protocols. Experiments were performed in triplicate. Soft agar anchorage independent colony formation assays were carried out as previously described[85]. After 2 weeks of growth, cells were fixed in 10% formalin containing 0.005% Crystal Violet for 1 hour at room temperature. Formalin was removed and colonies were imaged on a Leica S8 AP0 microscope. Twelve images per cell line were taken and automated colony counts were done using ImageJ software.

FOXR2 overexpression construct

FOXR2 cDNA (Open Biosystems) was cloned into the Gateway Vector System (Invitrogen) and subcloned into a *piggyBac* (*PB*) transposon vector. The *PB* control vector contains the *Luciferase* and *Gfp* reporter genes. Cells were transfected with 2ug of *FOXR2* or *Luciferase PB* transposon (Supplementary Fig. 8a) and 500ng of PB7 transposase plasmid using the NEON transfection system following manufacturers protocols (Invitrogen). Successfully transfected cells were enriched with 1ug/ml puromycin.

Generation of TALEN Knockout Cell Lines

TALENs targeting *FOXR2* were designed using TALE-NT and constructed as previously described[86–88]. An *HPRT* TALEN pair served as a control[86]. TALENs were assembled using Golden Gate cloning with the truncated 152+63 TALEN backbone[86,89]. Assembled TALENs were tested by transient transfection into K562 cells using the NEON electroporation system (Invitrogen) and subsequent CEL-I assay[90].

Knockout cell lines were generated using the *PB* Co-transposition method (*Moriarity et al.*, unpublished data). Briefly, cells were electroporated with plasmids encoding the left and right TALENs, the hyperactive *PB7* transposase, and Puromycin encoding transposon vectors. TALEN-treated cells were incubated at 37°C, 5% CO2 for 1 day followed by two days of 'cold shock' at 30°C to increase nuclease activity[91]. Cells were seeded at 50 cells per well in 96 well plates with Puromycin containing DMEM. Single cell clones were expanded, DNA was extracted, and CEL-I PCR was performed with amplicons sequenced via standard single pass Sanger sequencing (ACGT, Inc). Individual clone sequence data were analyzed for insertion/deletions (indels) formed by non-homologous end joining at the TALEN cut site and were classified as wildtype (WT), knockout (KO), or mutation detected (MD). Mutation detected clones were further analyzed by standard TOPO cloning and sequencing to determine the indels at each allele.

Quantitative-PCR analysis

1ug of total RNA was DNase (Life Technologies) treated and used for reverse transcription with the Super Script III first strand synthesis kit (Life Technologies) following manufacturer's protocol. qPCR reactions utilized the LightCycler 480 SYBR I Green (Roche) and were analyzed on an Eppendorf Mastercycler ep gradient S. Primers are listed in Supplementary Table 12. Data were analyzed using the RealPlex software, calibrated to *ACTB* levels, and normalized to respective controls.

Immunoblotting and immunofluorescence

FOXR2 protein was detected in whole cell lysates harvested with modified RIPA buffer (0.5% (vol/vol) NP-40, 50 mM Tris-HCl pH 7.4, 150 mM NaCl, 1 mM EDTA) containing phosphatase inhibitors (SIGMA) and a complete mini protease inhibitor pellet (Roche). Lysates were separated on a 10% resolving gel, transferred to PVDF membrane, and probed with antibodies against FOXR2 (SIGMA) and GAPDH (Cell Signaling Tech.) following manufacturers' protocols. Immunofluorescence on tissue sections and cell lines with antibodies probing FOXR2 (SIGMA) and CNPase (Santa Cruz) were carried out following manufacturers' protocols followed by incubation with fluorescently labeled secondary antibodies (Life Technologies). Slides were counter stained and mounted with anti-FADE Gold (Life Technologies) containing DAPI. Images were acquired using AxioVision software.

Supplementary Material

Refer to Web version on PubMed Central for supplementary material.

Acknowledgments

References

1. Ducatman BS, Scheithauer BW, Piepgras DG, Reiman HM, Ilstrup DM. Malignant peripheral nerve sheath tumors. A clinicopathologic study of 120 cases. Cancer. 1986; 57:2006–21. [PubMed: 3082508]

2. Evans DG, et al. Malignant peripheral nerve sheath tumours in neurofibromatosis 1. Journal of medical genetics. 2002; 39:311–4. [PubMed: 12011145]

3. Watson MA, et al. Gene Expression Profiling Reveals Unique Molecular Subtypes of Neurofibromatosis Type I-associated and Sporadic Malignant Peripheral Nerve Sheath Tumors. Brain pathology. 2004; 14:297–303. [PubMed: 15446585]

4. Holtkamp N, et al. Subclassification of nerve sheath tumors by gene expression profiling. Brain pathology. 2004; 14:258–264. [PubMed: 15446580]

5. Miller SJ, et al. Large-scale molecular comparison of human schwann cells to malignant peripheral nerve sheath tumor cell lines and tissues. Cancer Res. 2006; 66:2584. [PubMed: 16510576]

6. Zou C, et al. Clinical, pathological, and molecular variables predictive of malignant peripheral nerve sheath tumor outcome. Annals of surgery. 2009; 249:1014–22. [PubMed: 19474676]

7. Messiaen LM, et al. Exhaustive mutation analysis of the NF1 gene allows identification of 95% of mutations and reveals a high frequency of unusual splicing defects. Hum Mutat. 2000; 15:541–555. [PubMed: 10862084]

8. Leppig KA, et al. Familial neurofibromatosis 1 microdeletions: cosegregation with distinct facial phenotype and early onset of cutaneous neurofibromata. Am J Med Genet. 1998; 73:197–204. [PubMed: 9409873]

9. De Raedt T, et al. Elevated Risk for MPNST in< i> NF1 Microdeletion Patients. The American Journal of Human Genetics. 2003; 72:1288–1292.

10. Ballester R, et al. The NF1 locus encodes a protein functionally related to mammalian GAP and yeast IRA proteins. Cell. 1990; 63:851–9. [PubMed: 2121371]

11. Sherman LS, Atit R, Rosenbaum T, Cox AD, Ratner N. Single cell Ras-GTP analysis reveals altered Ras activity in a subpopulation of neurofibroma Schwann cells but not fibroblasts. J Biol Chem. 2000; 275:30740. [PubMed: 10900196]

12. Basu TN, et al. Aberrant Regulation Of Ras Proteins In Malignant-tumor Cells From Type-1 Neurofibromatosis Patients. Nature. 1992; 356:713–715. [PubMed: 1570015]

13. Cichowski K, Jacks T. NF1 tumor suppressor gene function: narrowing the GAP. Cell. 2001; 104:593–604. [PubMed: 11239415]

14. Forus A, et al. Comparative genomic hybridization analysis of human sarcomas: I. Occurrence of genomic imbalances and identification of a novel major amplicon at 1q21-q22 in soft tissue sarcomas. Genes, chromosomes & cancer. 1995; 14:8–14. [PubMed: 8527390]

15. Lothe RA, et al. Gain of 17q24-qter detected by comparative genomic hybridization in malignant tumors from patients with von Recklinghausen's neurofibromatosis. Cancer research. 1996; 56:4778–81. [PubMed: 8840998]

16. Mechtersheimer G, et al. Analysis of chromosomal imbalances in sporadic and NF1-associated peripheral nerve sheath tumors by comparative genomic hybridization. Genes, chromosomes & cancer. 1999; 25:362–9. [PubMed: 10398430]

17. Mertens F, et al. Cytogenetic findings in malignant peripheral nerve sheath tumors. International journal of cancer. 1995; 61:793–8.

18. Plaat BE, et al. Computer-assisted cytogenetic analysis of 51 malignant peripheral-nerve-sheath tumors: sporadic vs. neurofibromatosis-type-1-associated malignant schwannomas. International journal of cancer. 1999; 83:171–8.

19. Schmidt H, et al. Genomic imbalances of 7p and 17q in malignant peripheral nerve sheath tumors are clinically relevant. Genes, chromosomes & cancer. 1999; 25:205–11. [PubMed: 10379866]

20. Schmidt H, et al. Gains in chromosomes 7, 8q, 15q and 17q are characteristic changes in malignant but not in benign peripheral nerve sheath tumors from patients with Recklinghausen's disease. Cancer letters. 2000; 155:181–90. [PubMed: 10822134]

21. Schmidt H, et al. Cytogenetic characterization of six malignant peripheral nerve sheath tumors: comparison of karyotyping and comparative genomic hybridization. Cancer genetics and cytogenetics. 2001; 128:14–23. [PubMed: 11454424]

22. Birindelli S, et al. Rb and TP53 pathway alterations in sporadic and NF1-related malignant peripheral nerve sheath tumors. Laboratory investigation; a journal of technical methods and pathology. 2001; 81:833–44.

23. Legius E, et al. TP53 mutations are frequent in malignant NFI tumors. Genes, Chromosomes and Cancer. 2006; 10:250–255. [PubMed: 7522538]

24. Perry A, et al. Differential NF1, p16, and EGFR patterns by interphase cytogenetics (FISH) in malignant peripheral nerve sheath tumor (MPNST) and morphologically similar spindle cell neoplasms. Journal of neuropathology and experimental neurology. 2002; 61:702–9. [PubMed: 12152785]

25. Menon A, et al. Chromosome 17p deletions and p53 gene mutations associated with the formation of malignant neurofibrosarcomas in von Recklinghausen neurofibromatosis. Proc Natl Acad Sci U S A. 1990; 87:5435. [PubMed: 2142531]

26. Kourea HP, Orlow I, Scheithauer BW, Cordon-Cardo C, Woodruff JM. Deletions of the INK4A gene occur in malignant peripheral nerve sheath tumors but not in neurofibromas. Am J Pathol. 1999; 155:1855. [PubMed: 10595915]

27. Nielsen GP, et al. Malignant transformation of neurofibromas in neurofibromatosis 1 is associated with CDKN2A/p16 inactivation. Am J Pathol. 1999; 155:1879. [PubMed: 10595918]

28. Mantripragada KK, et al. High-resolution DNA copy number profiling of malignant peripheral nerve sheath tumors using targeted microarray-based comparative genomic hybridization. Clinical Cancer Research. 2008; 14:1015. [PubMed: 18281533]

29. Mawrin C, et al. Immunohistochemical and molecular analysis of p53, RB, and PTEN in malignant peripheral nerve sheath tumors. Virchows Archiv. 2002; 440:610–615. [PubMed: 12070601]

30. Holtkamp N, et al. Mutation and expression of PDGFRA and KIT in malignant peripheral nerve sheath tumors, and its implications for imatinib sensitivity. Carcinogenesis. 2006; 27:664. [PubMed: 16357008]

31. Storlazzi C, et al. Identification of a novel amplicon at distal 17q containing the BIRC5/ SURVIVIN gene in malignant peripheral nerve sheath tumours. J Pathol. 2006; 209:492–500. [PubMed: 16721726]

32. Badache A, De Vries GH. Neurofibrosarcoma-derived Schwann cells overexpress platelet-derived growth factor (PDGF) receptors and are induced to proliferate by PDGF BB. J Cell Physiol. 1998; 177:334–342. [PubMed: 9766530]

33. Badache A, Muja N, De Vries GH. Expression of Kit in neurofibromin-deficient human Schwann cells: role in Schwann cell hyperplasia associated with type 1 neurofibromatosis. Oncogene. 1998; 17:795–800. [PubMed: 9715282]

34. Keng VW, et al. A conditional transposon-based insertional mutagenesis screen for genes associated with mouse hepatocellular carcinoma. Nature biotechnology. 2009; 27:264–74.

35. Dupuy AJ, et al. A modified sleeping beauty transposon system that can be used to model a wide variety of human cancers in mice. Cancer research. 2009; 69:8150–6. [PubMed: 19808965]

36. Wu X, et al. Clonal selection drives genetic divergence of metastatic medulloblastoma. Nature. 2012; 482:529–533. [PubMed: 22343890]

37. Quintana RM, et al. A Transposon-Based Analysis of Gene Mutations Related to Skin Cancer Development. J Invest Dermatol. 2012

38. Lappe-Siefke C, et al. Disruption of Cnp1 uncouples oligodendroglial functions in axonal support and myelination. Nature genetics. 2003; 33:366–74. [PubMed: 12590258]

39. Tabone-Eglinger S, et al. Frequent EGFR Positivity and Overexpression in High-Grade Areas of Human MPNSTs. Sarcoma. 2008; 2008:849156. [PubMed: 18769552]

40. Holtkamp N, et al. MMP-13 and p53 in the progression of malignant peripheral nerve sheath tumors. Neoplasia (New York, N Y. 2007; 9:671–7.

41. Ling BC, et al. Role for the epidermal growth factor receptor in neurofibromatosis-related peripheral nerve tumorigenesis. Cancer cell. 2005; 7:65–75. [PubMed: 15652750]

42. de Vries A, et al. Targeted point mutations of p53 lead to dominant-negative inhibition of wild-type p53 function. Proceedings of the National Academy of Sciences of the United States of America. 2002; 99:2948–53. [PubMed: 11867759]

43. Carli M, et al. Pediatric malignant peripheral nerve sheath tumor: the Italian and German soft tissue sarcoma cooperative group. Journal of Clinical Oncology. 2005; 23:8422–8430. [PubMed: 16293873]

44. Stucky CCH, et al. Malignant peripheral nerve sheath tumors (MPNST): the Mayo Clinic experience. Annals of surgical oncology. 2012; 19:878–885. [PubMed: 21861229]

45. Pytel P, Taxy JB, Krausz T. Divergent differentiation in malignant soft tissue neoplasms: the paradigm of liposarcoma and malignant peripheral nerve sheath tumor. International journal of surgical pathology. 2005; 13:19–28. [PubMed: 15735851]

46. Magro G, et al. Multinucleated floret-like giant cells in sporadic and NF1-associated neurofibromas: a clinicopathologic study of 94 cases. Virchows Arch. 456:71–6. [PubMed: 19937344]

47. Rodriguez FJ, Folpe AL, Giannini C, Perry A. Pathology of peripheral nerve sheath tumors: diagnostic overview and update on selected diagnostic problems. Acta Neuropathol. 2012:1–25.

48. Collier LS, Carlson CM, Ravimohan S, Dupuy AJ, Largaespada DA. Cancer gene discovery in solid tumours using transposon-based somatic mutagenesis in the mouse. Nature. 2005; 436:272–6. [PubMed: 16015333]

49. Sarver A, Erdman J, Starr T, Largaespada D, Silverstein KA. TAPDANCE: An Automated tool to identify and annotate Transposon insertion CISs and associations between CISs from next generation sequence data. BMC Bioinformatics. 2012; 13:154. [PubMed: 22748055]

50. Brett BT, et al. Novel molecular and computational methods improve the accuracy of insertion site analysis in Sleeping Beauty-induced tumors. PloS one. 2011; 6:e24668. [PubMed: 21931803]

51. Gregorian C, et al. PTEN dosage is essential for neurofibroma development and malignant transformation. Proceedings of the National Academy of Sciences of the United States of America. 2009; 106:19479–84. [PubMed: 19846776]

52. Largaespada DA, Collier LS. Transposon-mediated mutagenesis in somatic cells: identification of transposon-genomic DNA junctions. Methods in molecular biology (Clifton, N J. 2008; 435:95–108.

53. Feber A, et al. Comparative methylome analysis of benign and malignant peripheral nerve sheath tumors. Genome Res. 2011; 21:515–524. [PubMed: 21324880]

54. Yang J, et al. Genomic and molecular characterization of malignant peripheral nerve sheath tumor identifies the IGF1R pathway as a primary target for treatment. Clinical Cancer Research. 2011; 17:7563–7573. [PubMed: 22042973]

55. Forbes SA, et al. COSMIC: mining complete cancer genomes in the Catalogue of Somatic Mutations in Cancer. Nucleic Acids Res. 2011; 39:D945–D950. [PubMed: 20952405]

56. Ghadimi MP, et al. Targeting the PI3K/mTOR Axis, Alone and in Combination with Autophagy Blockade, for the Treatment of Malignant Peripheral Nerve Sheath Tumors. Molecular Cancer Therapeutics. 2012; 11:1758–1769. [PubMed: 22848094]

57. Saito T, et al. Nuclear< i> β-catenin correlates with cyclin D1 expression in spindle and pleomorphic sarcomas but not in synovial sarcoma. Hum Pathol. 2006; 37:689–697. [PubMed: 16733209]

58. Mo W, et al. CXCR4/CXCL12 Mediate Autocrine Cell-Cycle Progression in NF1-Associated Malignant Peripheral Nerve Sheath Tumors. Cell. 2013

59. Keng VW, et al. PTEN and NF1 Inactivation in Schwann Cells Produces a Severe Phenotype in the Peripheral Nervous System That Promotes the Development and Malignant Progression of Peripheral Nerve Sheath Tumors. Cancer Res. 2012; 72:3405–3413. [PubMed: 22700876]

60. Starr TK, et al. A transposon-based genetic screen in mice identifies genes altered in colorectal cancer. Science (New York, N Y. 2009; 323:1747–50.

61. Jessen KR. Glial cells. Int J Biochem Cell Biol. 2004; 36:1861–1867. [PubMed: 15203098]

62. Pérez-Mancera PA, et al. The deubiquitinase USP9X suppresses pancreatic ductal adenocarcinoma. Nature. 2012; 486:266–270. [PubMed: 22699621]

63. Subramanian S, et al. Genome-wide transcriptome analyses reveal p53 inactivation mediated loss of miR-34a expression in malignant peripheral nerve sheath tumours. J Pathol. 2010; 220:58–70. [PubMed: 19890883]

64. Je EM, An CH, Yoo NJ, Lee SH. Mutational analysis of PIK3CA, JAK2, BRAF, FOXL2, IDH1, AKT1 and EZH2 oncogenes in sarcomas. APMIS. 2012

65. Jacks T, et al. Tumour predisposition in mice heterozygous for a targeted mutation in Nf1. Nat Genet. 1994; 7:353–361. [PubMed: 7920653]

66. Cichowski K, et al. Mouse models of tumor development in neurofibromatosis type 1. Science (New York, N Y. 1999; 286:2172–6.

67. Zhu Y, Ghosh P, Charnay P, Burns DK, Parada LF. Neurofibromas in NF1: Schwann cell origin and role of tumor environment. Science (New York, N Y. 2002; 296:920–2.

68. Wu J, et al. Plexiform and dermal neurofibromas and pigmentation are caused by Nf1 loss in desert hedgehog-expressing cells. Cancer Cell. 2008; 13:105–116. [PubMed: 18242511]

69. Katoh M. Identification and characterization of human FOXN6, mouse Foxn6, and rat Foxn6 genes in silico. Int J Oncol. 2004; 25:219. [PubMed: 15202009]

70. Santo E, et al. Oncogenic activation of FOXR1 by 11q23 intrachromosomal deletion-fusions in neuroblastoma. Oncogene. 2011; 31:1571–1581. [PubMed: 21860421]

71. Uhlen M, et al. Towards a knowledge-based human protein atlas. Nat Biotechnol. 2010; 28:1248–1250. [PubMed: 21139605]

72. Rhodes DR, et al. ONCOMINE: a cancer microarray database and integrated data-mining platform. Neoplasia (New York, NY). 2004; 6:1.

73. Rhodes DR, et al. Oncomine 3.0: genes, pathways, and networks in a collection of 18,000 cancer gene expression profiles. Neoplasia (New York, NY). 2007; 9:166.

74. Myatt SS, Lam EWF. The emerging roles of forkhead box (Fox) proteins in cancer. Nature Reviews Cancer. 2007; 7:847–859.

75. Stemmer-Rachamimov AO, et al. Comparative pathology of nerve sheath tumors in mouse models and humans. Cancer Res. 2004; 64:3718–3724. [PubMed: 15150133]

76. Dai M, et al. Evolving gene/transcript definitions significantly alter the interpretation of GeneChip data. Nucleic Acids Res. 2005; 33:e175–e175. [PubMed: 16284200]

77. Benjamini Y, Hochberg Y. Controlling the false discovery rate: a practical and powerful approach to multiple testing. Journal of the Royal Statistical Society Series B (Methodological). 1995:289–300.

78. Irizarry RA, et al. The human colon cancer methylome shows similar hypo-and hypermethylation at conserved tissue-specific CpG island shores. Nat Genet. 2009; 41:178–186. [PubMed: 19151715]

79. Yang J, et al. Deletion of the< i> WWOX gene and frequent loss of its protein expression in human osteosarcoma. Cancer Lett. 2010; 291:31–38. [PubMed: 19896763]

80. Olshen AB, Venkatraman E, Lucito R, Wigler M. Circular binary segmentation for the analysis of array-based DNA copy number data. Biostatistics. 2004; 5:557–572. [PubMed: 15475419]

81. Van De Wiel MA, et al. CGHcall: calling aberrations for array CGH tumor profiles. Bioinformatics. 2007; 23:892–894. [PubMed: 17267432]

82. Sun W, et al. Integrated study of copy number states and genotype calls using high-density SNP arrays. Nucleic Acids Res. 2009; 37:5365–5377. [PubMed: 19581427]

83. DeRycke MS, et al. S100A1 expression in ovarian and endometrial endometrioid carcinomas is a prognostic indicator of relapse-free survival. Am J Clin Pathol. 2009; 132:846–856. [PubMed: 19926575]

84. Rizzardi A, et al. Quantitative comparison of immunohistochemical staining measured by digital image analysis versus pathologist visual scoring. Diagnostic Pathology. 2012; 7:42. [PubMed: 22515559]

85. Daniel AR, Faivre EJ, Lange CA. Phosphorylation-dependent antagonism of sumoylation derepresses progesterone receptor action in breast cancer cells. Molecular Endocrinology. 2007; 21:2890–2906. [PubMed: 17717077]

86. Cermak T, et al. Efficient design and assembly of custom TALEN and other TAL effector-based constructs for DNA targeting. Nucleic Acids Res. 2011; 39:e82–e82. [PubMed: 21493687]

87. Wood AJ, et al. Targeted genome editing across species using ZFNs and TALENs. Science. 2011; 333:307–307. [PubMed: 21700836]

88. Mussolino C, et al. A novel TALE nuclease scaffold enables high genome editing activity in combination with low toxicity. Nucleic Acids Res. 2011; 39:9283–9293. [PubMed: 21813459]

89. Miller JC, et al. A TALE nuclease architecture for efficient genome editing. Nat Biotechnol. 2010; 29:143–148. [PubMed: 21179091]

90. Guschin DY, et al. A rapid and general assay for monitoring endogenous gene modification. Methods Mol Biol. 2010; 649:247–256. [PubMed: 20680839]

91. Doyon Y, et al. Transient cold shock enhances zinc-finger nuclease–mediated gene disruption. Nature methods. 2010; 7:459–460. [PubMed: 20436476]
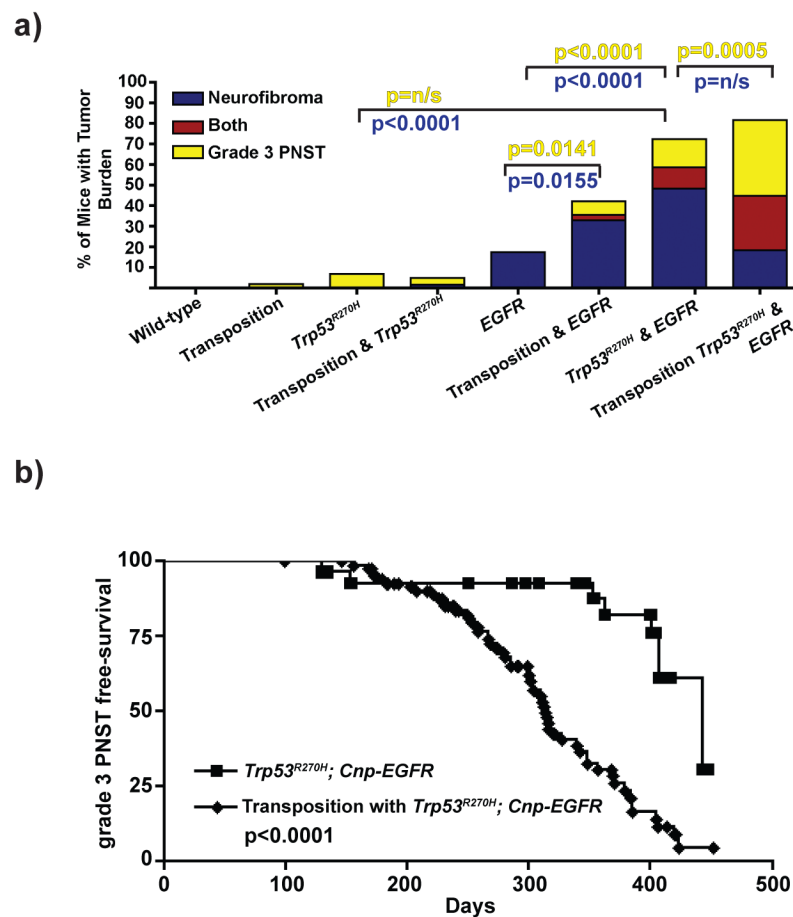
Figure 1. *SB* **mutagenesis induced and accelerated grade 3 PNST formation**
(a) Bar graph depicting the percentage of mice that developed each tumor type at the time of necropsy based on genotype. p-values reflect FET. (b) Survival curve depicting incidence of grade 3 tumor formation in $Trp53^{R270H}$; $Cnp\text{-}EGFR$ control mice compared to mice undergoing transposition with $Trp53^{R270H}$; $Cnp\text{-}EGFR$ background. Median age of tumor-free survival was 313 days (n=87) with transposition compared to 443 days (n=29) in the control. Log rank test: p<0.0001.
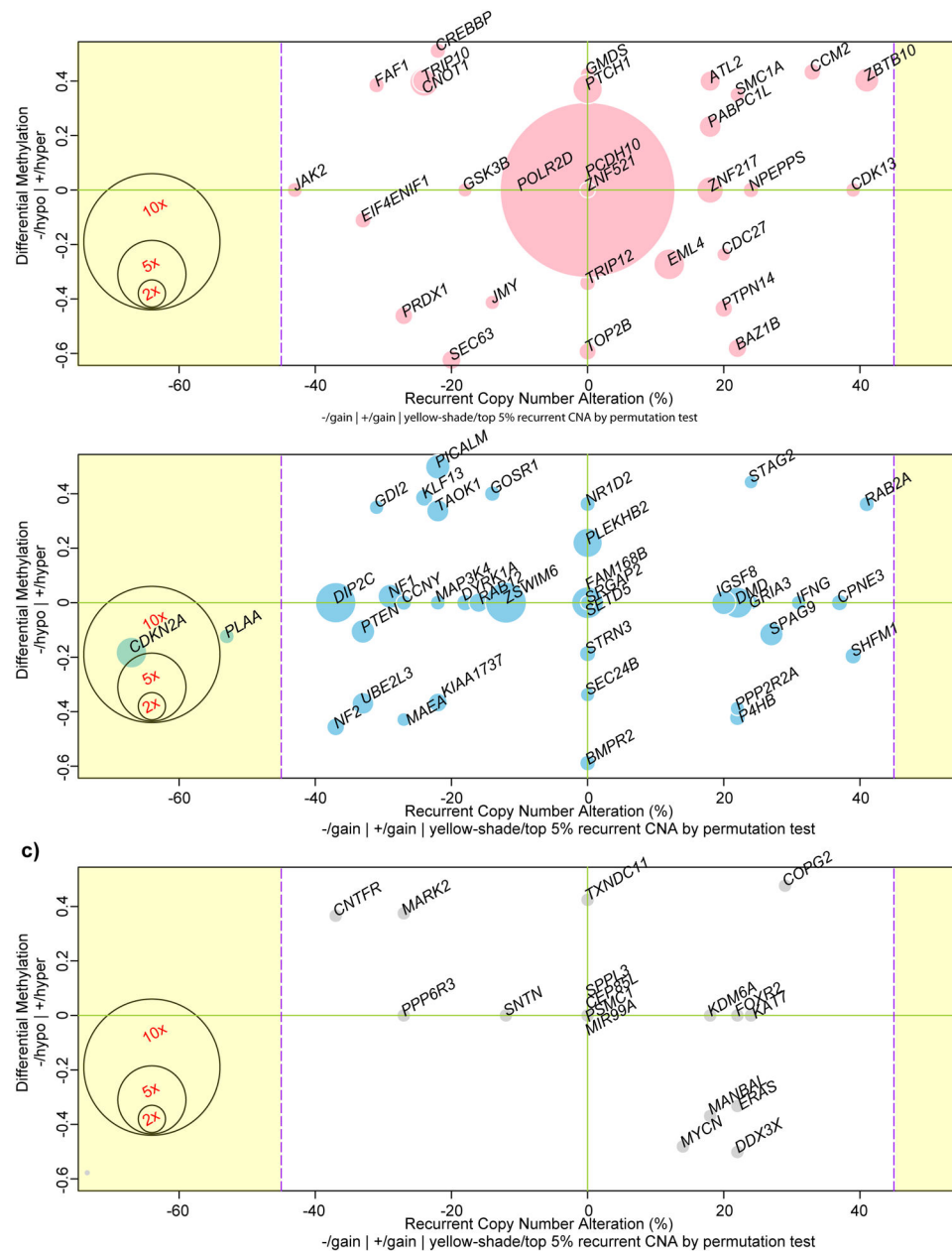
Figure 2. Comparative analysis of grade 3 PNST CISs to human MPNSTs

CNA, methylome, and microarray expression data from human MPNST data (Supplementary Fig. 6–8, Supplementary Tables 3,5) were combined into a "bubble plot". The y-axis displays the methylation state (negative number indicating hypomethylation and positive number indicating hypermethylation) of each gene's CpG-IS nearest to the transcriptional start site (TSS) in MPNSTs versus NHSCs (methylation analysis described in detail in online methods and Supp Table 5). The x-axis depicts the CNA observed in MPNSTs versus NHSCs (determination of CNA is described in online methods and Supp Table 3). Numbers reflect the percentage of the 51 patient samples that have a CNA. Negative numbers indicated CNA loss while positive numbers indicate CNA gains. The

yellow shaded area indicates the 95th percentile for significant recurrent CNAs. Microarray expression was represented by size from 1X-10X (determination of expression changes are described in online methods and Supp Fig 8) and color to depict genes that are upregulated in red (a), downregulated in blue (b), or have no change or have no probes on the microarray in gray (c) in gene expression comparing MPNSTs to NHSCs. For recurrent CNAs, we considered a gene that shows the gain (or loss) pattern if the ratio of gain (or loss) out of all 51 patients is more than 1.5X that of the ratio of loss (or gain). Significant recurrent CNAs must be observed in 23/51 patient samples (95th percentile).

a)

b)
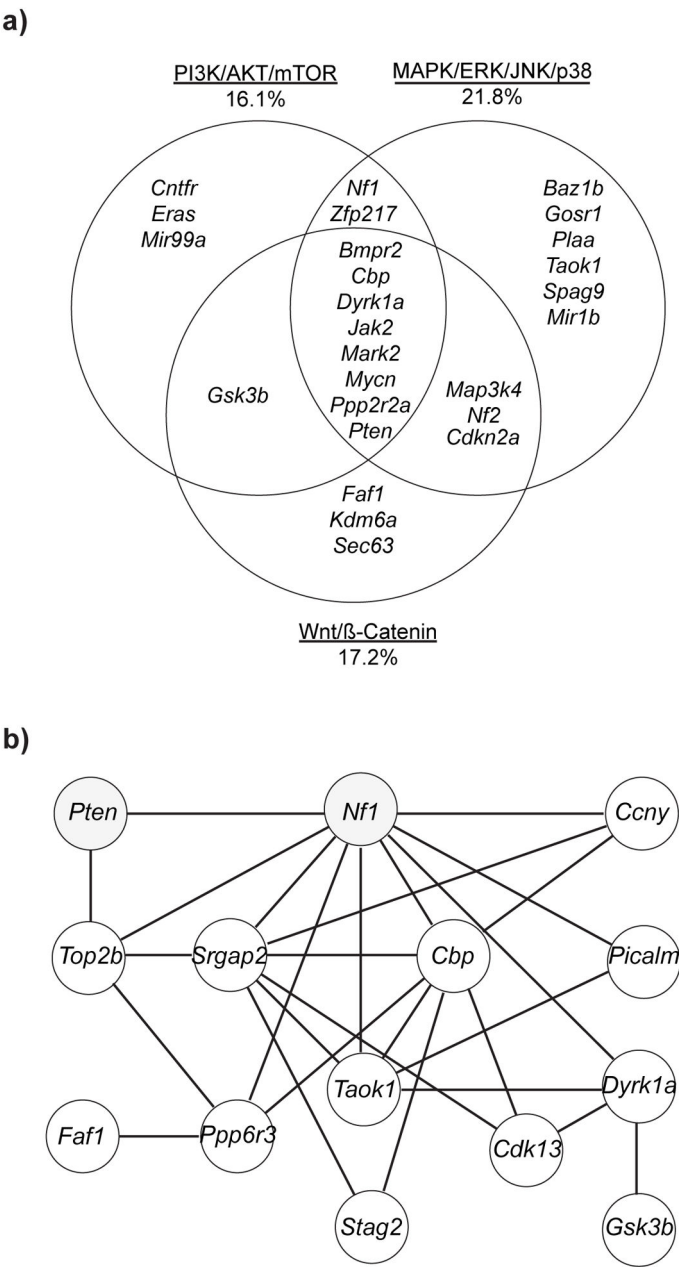
Figure 3. CIS analysis for cooperating genes and pathways for grade 3 PNST formation
(a) Venn diagram depicting the clustering of the 87 grade 3 PNST CISs into three cancer-associated signaling pathways: PI3K/AKT/mTOR, MAPK/ERK/p38, Wnt/CTNNB1. Values indicate the percentage of the 87 CISs contributing to each pathway. CISs were classified into each pathway based on IPA, DAVID, GENECARD, and PUBMED analysis and literature review to identify canonical members and pathway effectors. (b) This module of genes depicts co-occurrence analysis of grade 3 PNST td-CISs. p-values for CIS interactions are listed in Supplementary Table 10.

a)

b)

c)

d)
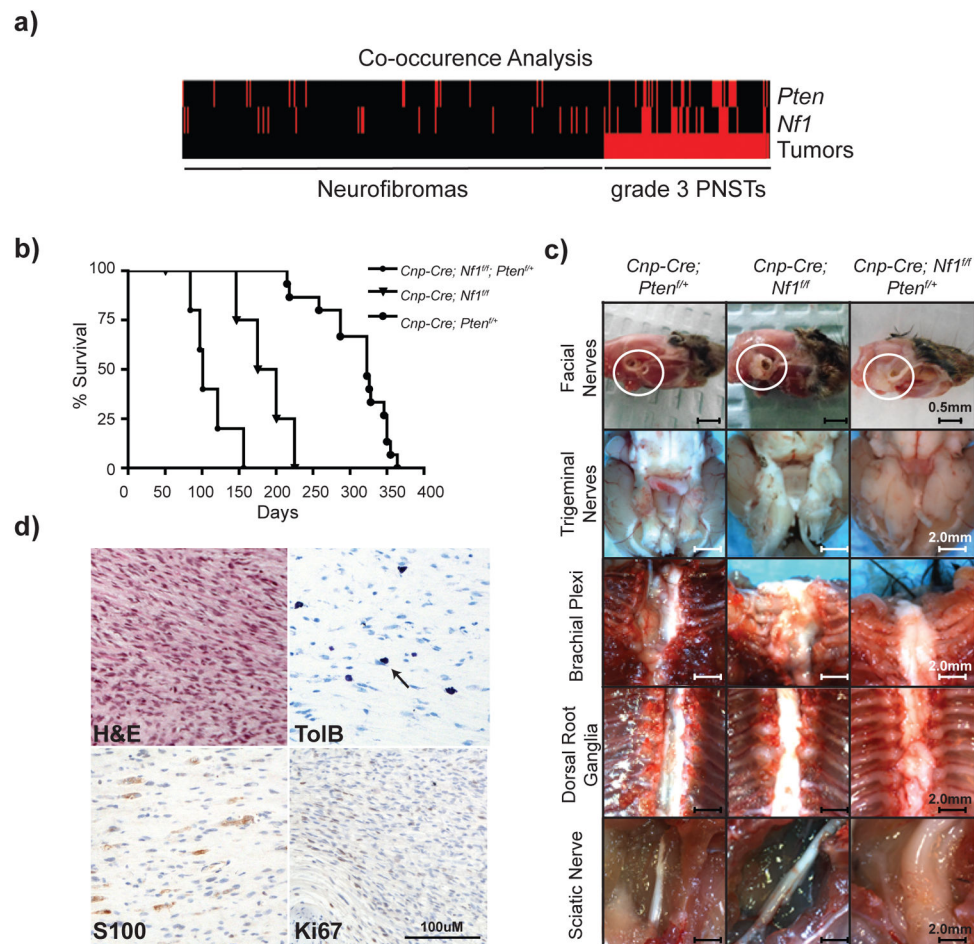
Figure 4. Loss of *Nf1* and *Pten* cooperate to form high-grade PNSTs

(a) Co-occurrence analysis heat map depicting each mouse tumor (neurofibromas left, grade 3 PNST right) and the presence of an insertion into either the *Pten* or the *Nf1* locus (red bars). Tumors from 13/62 mice (106 grade 3 PNSTS) contained insertions in both *Nf1* and *Pten*, which is statistically significantly different from the neurofibroma profile of 1/55 mice (269 neurofibromas) (FET p<7.94x10^{-05}). (b) Survival curve of three genetic cohorts: *Cnp-Cre; Nf1$^{f/f}$; Pten$^{f/+}$*(n=5), *Cnp-Cre; Nf1$^{f/f}$* (n=5), *Cnp-Cre; Pten$^{f/+}$*(n=15). Statistical analysis of curves: *Cnp-Cre; Nf1$^{f/f}$; Pten$^{f/+}$* vs *Cnp-Cre; Nf1$^{f/f}$* p<0.05; *Cnp-Cre; Nf1$^{f/f}$; Pten$^{f/+}$* vs *Cnp-Cre; Pten$^{f/+}$*p<0.0001; *Cnp-Cre; Nf1$^{f/f}$* vs *Cnp-Cre; Pten$^{f/+}$*p=0.0018. p-values reflect Logrank test. (c) Necropsy images from a 275 day old *Cnp-Cre; Pten$^{f/+}$*mouse, a 175 day old *Cnp-Cre; Nf1$^{f/f}$* mouse, and a 120 day old *Cnp-Cre; Nf1$^{f/f}$; Pten$^{f/+}$*mouse. (d) Histological analysis of sciatic nerve tumor in (c). H&E staining depicts high cellularity with few mitotic figures corroborated with Ki67 IHC. Toluidine blue stain depicts presence of Mast cells indicative of nerve origin. S100 positive staining depicts presence of Schwann cells. This tumor contained regions of high-grade PNST formation.
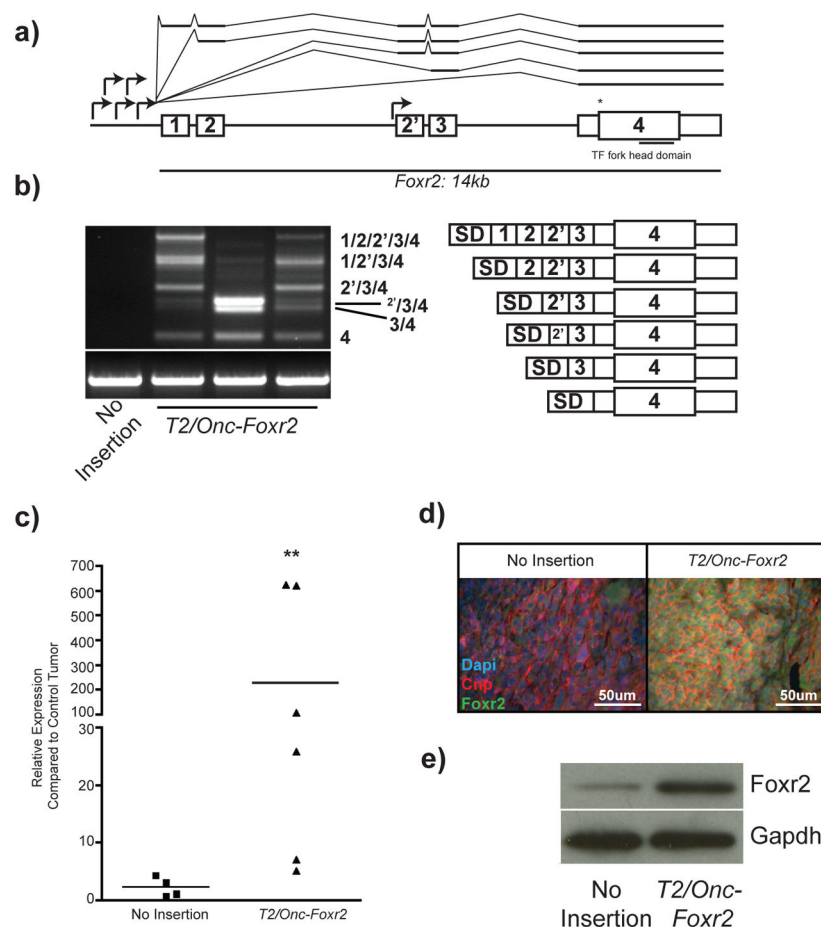
Figure 5. T2/Onc insertions in the *Foxr2* locus cause overexpression of *Foxr2* in SB-derived grade 3 PNSTs

(a) Schematic depicting the mouse *Foxr2* locus. The MSCV promoter of T2/Onc for all transposon insertions faces the same orientation as *Foxr2* transcription (arrows). Annotated exons are marked as 1, 2, 3, 4. * represents the translational start site. The exon 2′ is a putative unannotated exon. (b) RT-PCR on cDNA from *SB*-derived grade 3 PNSTs. Bands indicate mRNA fusions between T2/Onc and *Foxr2*. Lane 1 is an *SB*-derived grade 3 PNST that did not contain a *Foxr2* insertion. Lanes 2 and 4 are T2/Onc insertions upstream of exon 1. Lane 3 is the T2/Onc insertion immediately upstream of exon 2′. The schematics are the sequenced splicing events from each of the excised products. The superscript 2′ represents splicing into the putative 2′ exon. (c) Quantitative PCR for *Foxr2* expression in *SB*-derived grade 3 PNSTs with and without a T2/Onc insertion in *Foxr2*. ** $p<0.001$ based on two-tailed student t-test. (d) Immunofluorescent staining for Foxr2 (green), Cnp (red), and Dapi (blue) on tumor sections containing (right) and not containing (left) a T2/Onc insertion in *Foxr2*. (e) Western blot analysis for Foxr2 expression from two *SB*-derived tumor cell lines containing (right) and not containing (left) a *T2/Onc* insertion into *Foxr2*.
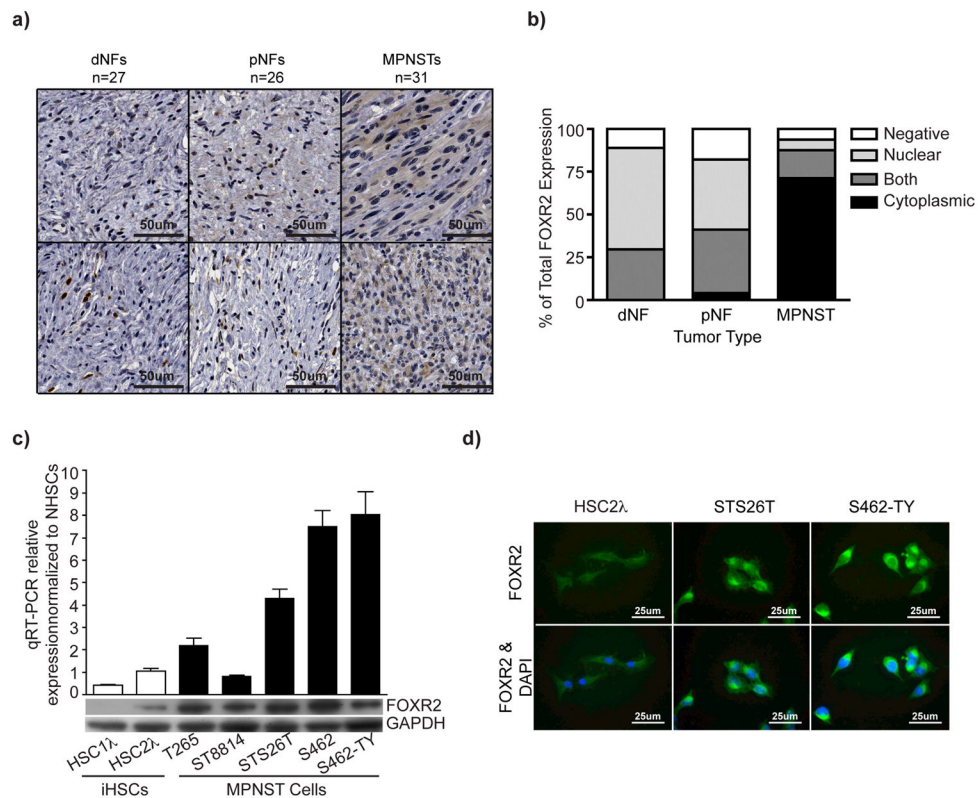
Figure 6. Increased *FOXR2* expression is associated with human MPNSTs

(a) Immunohistochemical staining for FOXR2 of a tissue microarray (TMA) containing 27 dermal neurofibroma samples (dNF), 26 plexiform neurofibroma samples (pNF), and 31 MPNST samples. Representative images for FOXR2 staining for each tumor type are shown. (b) Bar graph depicts percentages for either staining localization for each tumor type (nuclear, cytoplasmic, both, or negative). (c) The bar graph depicts quantitative PCR analysis for *FOXR2* expression in iHSCs (HSC1λ and HSC2λ) and MPNST (T265, ST8814, STS26T, S462, S462-TY) cell lines. Data are normalized to purified normal human Schwann cells (NHSCs). The lower bands indicate western blot analysis for FOXR2 for the same cell lines. (d) Immunofluorescent imaging of FOXR2 expression in HSC2λ, STS26T, and S462-TY. Staining is predominantly cytoplasmic as observed in the MPNST samples in (a).
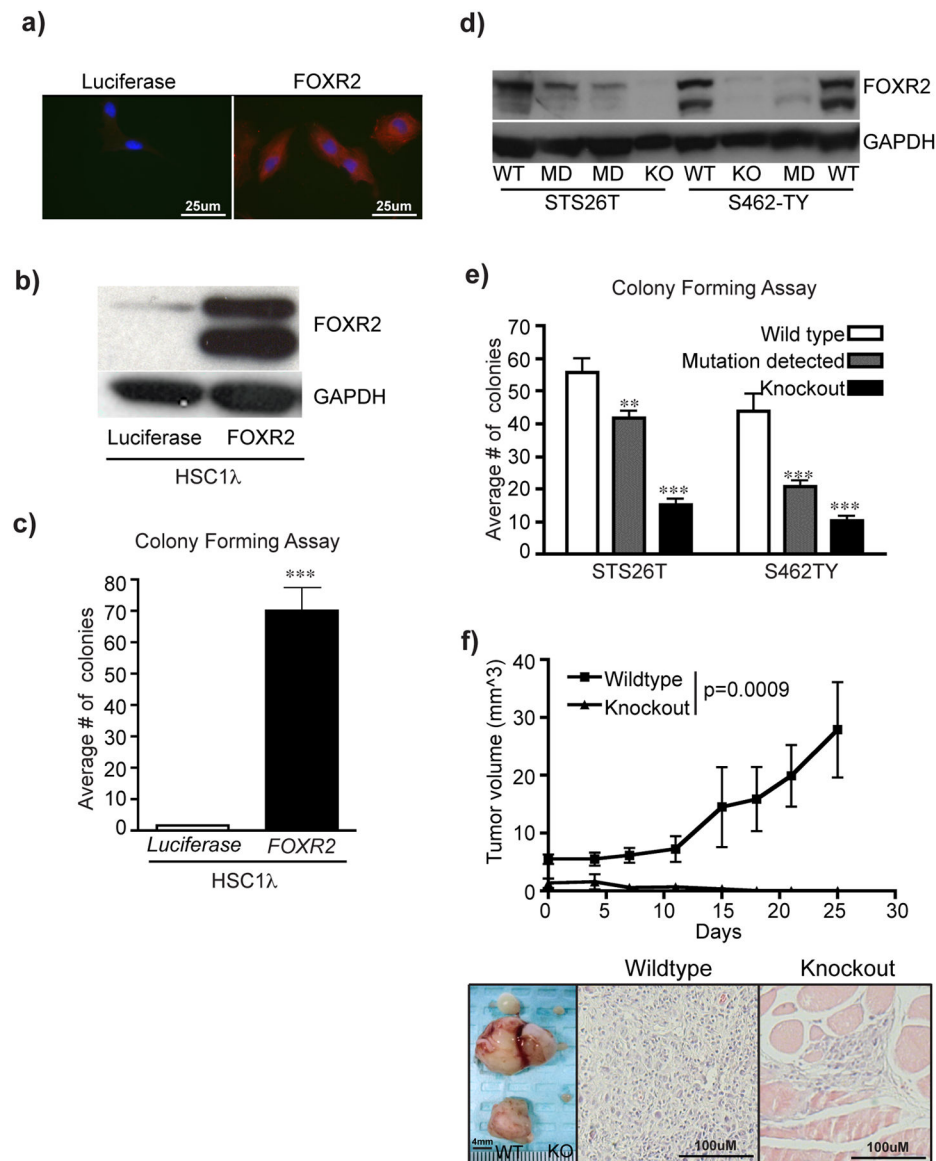
Figure 7. Modulating *FOXR2* expression significantly alters MPNST tumorigenic properties
(a) Immunofluorescent imaging of FOXR2 expression in HSC1λ targeted with either a
Luciferase expression construct (left) or a *FOXR2* expression construct (right). (b) FOXR2
western blot on cells from (a). (c) Bar graph depicts results from a soft-agar colony-forming
assay performed in triplicate. Statistical analysis was done using a two-tailed student t-test,
*** p<0.0001 (d) Western blot analysis of FOXR2 expression on STS26T and S462-TY cell
lines targeted with *FOXR2* TALENs. WT = wildtype, KO = knockout, MD = mutation
detected. (e) Bar graph depicts results from a soft agar colony-forming assay performed in
triplicate with biological replicate cell lines. STS26T wildtype (n= 3), STS26T mutation
detected (n=4), STS26T knockout (n=4), S462-TY wildtype (n=2), S462-TY mutation
detected (n=4), and S462-TY knockout (n=4). Statistics were done using a two-tailed
student t-test comparing to the respective wildtype control. **p-=0.0032, ***p<0.0001. (f)
One million STS26T wildtype (n=8, left flank) and STS26T *FOXR2* KO (n=8, right flank)

cells were injected into Nu/Nu mice. Tumors were measured over a 1 month period. Wildtype STS26T tumors grew significantly larger than paired KO (two-tailed student t-test ***p=0.0009). Images were captured at time of necropsy of the tumors from WT (n=5, left) or regions were injections occurred (n=5, right). H&E staining of tissue sections from the masses indicate the wildtype masses were tumors while the masses from the KO cells were predominantly fat pad tissue that contained the injected cells.

Table 1

List of grade 3 PNST CISs

This table is a combined list of CISs identified by the tdCIS method and the gCIS method. Twenty-two CIS were identified by both statistical analyses independently. p-values and q-values were generated as described by Sarver et al. 2012 and Brett et al. 2011. Prediction on gene function indicates if the T2/Onc insertion would cause transcriptional activation of a gene ("Drive" and "Drive N-terminal Truncation") or disrupt gene transcription ("Disrupt") based on position and orientation of T2/Onc insertion to gene transcription.

CIS-Associated Gene	% of Tumors with tdCIS	tdCIS P-Value library #	p-value for grade 3 PNST enrichment	% of Tumors with gCIS	gCIS q-Value library #	Prediction on gene function	Neurofibroma CIS	Human Homolog
Nf1	34.9	5.03×10^{-25}	8.04×10^{-06}	36.8	2.61×10^{-62}	Disrupt	X	NF1
Pten	30.2	3.21×10^{-41}	3.85×10^{-06}	31.1	0	Disrupt	X	PTEN
Stag2	19.8	6.72×10^{-12}	-	19.8	7.33×10^{-26}	Disrupt	X	STAG2
Taok1	19.8	1.32×10^{-18}	0.003062	19.8	6.41×10^{-49}	Disrupt	X	TAOK1
Srgap2	16.0	2.90×10^{-05}	0.001182	17.9	3.40×10^{-11}	Disrupt	X	SRGAP2
Faf1	14.2	0.047642812	0.03222	17.9	3.05×10^{-06}	Disrupt	X	FAF1
Crebbp	16.0	1.20×10^{-07}	0.002837	16.0	3.49×10^{-21}	Disrupt	X	CREBBP
Dyrk1a	11.3	1.44×10^{-06}	0.009831	11.3	1.48×10^{-09}	Disrupt	X	DYRK1A
Spag9	11.3	0.046952457	-	11.3	1.22×10^{-07}	Disrupt	X	SPAG9
Ppp6r3	10.4	0.047173607	-	10.4	7.46×10^{-09}	Disrupt	X	PPP6R3
Bmpr2	9.4	0.005118412	-	10.4	4.70×10^{-07}	Drive N-term truncation	-	BMPR2
Cdk13	9.4	0.005118412	0.01161	10.4	2.57×10^{-08}	Disrupt	X	CDK13
Ccny	4.7	0.042667588	-	10.4	4.25×10^{-06}	Drive N-term truncation	X	CCNY
Copg2	8.5	0.048819435	-	8.5	7.08×10^{-05}	Disrupt	X	COPG2
Eras	8.5	1.46×10^{-08}	-	8.5	1.20×10^{-74}	Drive N-term truncation	-	ERAS
gm9766	5.7	0.043383381	-	8.5	0.000234	Disrupt	X	C6orf204
Jak2	5.7	0.00127532	-	8.5	9.07×10^{-09}	Drive N-term truncation	X	JAK2
Sec63	7.5	0.047985716	-	7.5	1.28×10^{-05}	Disrupt	-	SEC63
Foxr2	6.6	3.27×10^{-05}	-	7.5	7.96×10^{-22}	Drive	-	FOXR2
Cnot1	5.7	0.043383381	-	7.5	7.14×10^{-05}	Disrupt	-	CNOT1
2610044O15Rik	4.7	0.042667588	-	5.7	5.60×10^{-11}	Drive N-term truncation	-	-

CIS-Associated Gene	% of Tumors with tdCIS	tdCIS P-Value library #	p-value for grade 3 PNST enrichment	% of Tumors with gCIS	gCIS q-Value library #	Prediction on gene function	Neurofibroma CIS	Human Homolog
Baz1b	4.7	0.042667588	0.0309	5.7	0.000157	Drive N-term truncation	-	*BAZ1B*
Cdc27	15.1	0.001665472	-	-	-	Disrupt	-	*CDC27*
Pcdh10	11.3	0.046952457	-	-	-	Disrupt	-	*PCDH10*
Top2b	11.3	0.046952457	-	-	-	Disrupt	X	*TOP2B*
Plaa	8.5	0.048819435	-	-	-	Disrupt	-	*PLAA*
Zfp521	8.5	0.048819435	-	-	-	Drive N-term truncation	-	*ZNF521*
Gdi2	7.5	0.047985716	-	-	-	Disrupt	X	*GDI2*
Gmds	7.5	0.047985716	-	-	-	Disrupt	-	*GMDS*
Gsk3b	7.5	0.047985716	-	-	-	Disrupt	X	*GSK3B*
Picalm	6.6	0.049919619	-	-	-	Disrupt	X	*PICALM*
Gria3	5.7	0.00127532	-	-	-	Disrupt	-	*GRIA3*
Jmy	5.7	0.043383381	-	-	-	Drive N-term truncation	-	*JMY*
Nf2	5.7	0.00127532	-	-	-	Disrupt	X	*NF2*
Dip2c	-	-	-	17.9	9.86×10^{-05}	Disrupt	X	*DIP2C*
Dmd	-	-	-	16.0	1.61×10^{-05}	Disrupt	X	*DMD*
Zswim6	-	-	-	11.3	1.40×10^{-06}	Disrupt	X	*ZSWIM6*
Kdm6a	-	-	-	10.4	6.11×10^{-05}	Disrupt	X	*KDM6A*
Eml4	-	-	-	9.4	9.21×10^{-05}	Disrupt	-	*EML4*
Trip12	-	-	-	9.4	9.41×10^{-05}	Disrupt	X	*TRIP12*
Npepps	-	-	-	7.5	3.95×10^{-06}	Drive	-	*NPEPPS*
Ptpn14	-	-	-	7.5	0.000211	Disrupt	-	*PTPN14*
Setd5	-	-	-	7.5	0.000103	Disrupt	X	*SETD5*
Smc1a	-	-	-	7.5	6.93×10^{-11}	Disrupt	-	*SMC1A*
Strn3	-	-	-	7.5	0.000448	Disrupt	X	*STRN3*
5830433M19Rik	-	-	-	6.6	0.000103	Disrupt	-	*C9orf82*
Cpne3	-	-	-	6.6	5.75×10^{-06}	Disrupt	-	*CPNE3*
Eif4enif1	-	-	-	6.6	1.24×10^{-08}	Disrupt	X	*EIF4ENIF1*
Map3k4	-	-	-	6.6	7.51×10^{-05}	Disrupt	-	*MAP3K4*

CIS-Associated Gene	% of Tumors with tdCIS	tdCIS P-Value library #	p-value for grade 3 PNST enrichment	% of Tumors with gCIS	gCIS q-Value library #	Prediction on gene function	Neurofibroma CIS	Human Homolog
Ppp2r2a	-	-	-	6.6	1.18×10^{-05}	Disrupt	X	PPP2R2A
Ptch1	-	-	-	6.6	1.28×10^{-09}	Disrupt	X	PTCH1
Rab2a	-	-	-	6.6	0.000438	Disrupt	X	RAB2A
Sec24b	-	-	-	6.6	0.000117	Disrupt	-	SEC24B
Sppl3	-	-	-	6.6	0.000178	Disrupt	-	SPPL3
Atl2	-	-	-	5.7	9.72×10^{-05}	Disrupt	-	ATL2
Fam168b	-	-	-	5.7	5.81×10^{-10}	Drive N-term truncation	X	FAM168B
Maea	-	-	-	5.7	4.65×10^{-08}	Disrupt	X	MAEA
Mark2	-	-	-	5.7	4.48×10^{-05}	Disrupt	X	MARK2
Shfm1	-	-	-	5.7	1.17×10^{-08}	Drive N-term truncation	-	SHFM1
Txndc11	-	-	-	5.7	0.000367	Disrupt	X	TXNDC11
Ube2l3	-	-	-	5.7	4.32×10^{-06}	Disrupt	X	UBE2L3
Ccm2	-	-	-	4.7	0.000296	Disrupt	-	CCM2
Cntfr	-	-	-	4.7	3.66×10^{-09}	Disrupt	-	CNTFR
Gosr1	-	-	-	4.7	8.84×10^{-05}	Disrupt	-	GOSR1
Klf13	-	-	-	4.7	7.38×10^{-05}	Disrupt	-	KLF13
Myst2	-	-	-	4.7	0.000131	Disrupt	-	KAT7
Nr1d2	-	-	-	4.7	0.000131	Disrupt	X	NR1D2
Plekhb2	-	-	-	4.7	1.55×10^{-06}	Disrupt	-	PLEKHB2
Rab12	-	-	-	4.7	6.99×10^{-08}	Disrupt	-	RAB12
Zbtb10	-	-	-	4.7	0.000292	Disrupt	-	ZBTB10
Zfp217	-	-	-	4.7	7.38×10^{-06}	Drive N-term truncation	-	ZNF217
2310044G17Rik	-	-	-	3.8	4.37×10^{-06}	Drive	-	KIAA1737
Cdkn2a	-	-	-	3.8	0.000128	Disrupt	-	CDKN2A
Ddx3x	-	-	-	3.8	3.07×10^{-05}	Disrupt	-	DDX3X
Manbal	-	-	-	3.8	0.000157	Drive	-	MANBAL
Mycn	-	-	-	3.8	8.71×10^{-12}	Disrupt	-	MYCN

CIS-Associated Gene	% of Tumors with tdCIS	tdCIS *P*-Value library #	p-value for grade 3 PNST enrichment	% of Tumors with gCIS	gCIS *q*-Value library #	Prediction on gene function	Neurofibroma CIS	Human Homolog
Pabpc1l	-	-	-	3.8	5.76×10^{-05}	Drive	-	*PABPC1L*
Prdx1	-	-	-	3.8	2.27×10^{-05}	Disrupt	-	*PRDX1*
Psmc1	-	-	-	3.8	1.66×10^{-08}	Disrupt	-	*PSMC1*
Sntn	-	-	-	3.8	4.48×10^{-05}	Disrupt	-	*SNTN*
2610507I01Rik	-	-	-	2.8	1.41×10^{-06}	Drive	-	-
Ifng	-	-	-	2.8	0.000154	Drive	-	*IFNG*
Igsf8	-	-	-	2.8	1.14×10^{-07}	Drive	-	*IGSF8*
Mir1b	-	-	-	2.8	0.000125	Disrupt	-	*MIR206*
Mir99a	-	-	-	2.8	1.61×10^{-05}	Drive	-	*MIR99A*
P4hb	-	-	-	2.8	0.000167	Disrupt	-	*P4HB*
Trip10	-	-	-	2.8	0.000104	Disrupt	-	*TRIP10*